Computation of diffuse scattering arising from one-phonon excitations in a neutron time-of-flight single crystal Laue diffraction experiment

Matthias J. GutmannAuthors

X**Matthias J. Gutmann**[a]*, **Gabriella Graziano**[ba], **Sanghamitra Mukhopadhyay**[a], **Keith Refson**[c] **and Martin v. Zimmermann**[d]

[a]ISIS Facility, Rutherford Appleton Laboratory, Chilton Didcot, Oxfordshire, OX11 0QX, UK

[b]Thomas Young Centre, London Centre for Nanotechnology and Department of Chemistry, University College London, London, WC1E 6BT, UK

[c]Computational Science and Engineering, Rutherford Appleton Laboratory, Chilton Didcot, Oxfordshire, OX11 0QX, UK

[d] Deutsches Elektronen Synchrotron DESY, Notkestr. 85, Hamburg, 22603, Germany

Correspondence email: matthias.gutmann@stfc.ac.uk

ynopsis   methodology is presented to compute 'inelastic diffraction' in a time-of-flight neutron single crystal Laue diffraction experiment from DFT results and illustrated using NaCl as an example.

bstract   Direct phonon excitation in a neutron time-of-flight single crystal Laue diffraction experiment has been observed in a single crystal of NaCl. At room temperature both phonon emission and excitation leave characteristic features in the diffuse scattering and these are well reproduced using ab-initio phonons from density-functional theory (DFT). A measurement at 20K illustrates the effect of thermal population of the phonons leaving the features corresponding to phonon excitation and strongly suppressing the phonon annihilation. A receipe is given to compute these effects combining DFT results with the geometry of the neutron experiment.

1. Introduction

The most common type of diffuse scattering at room-temperature in a single crystal diffraction experiment designed to measure it is caused by lattice vibrations and is known as thermal diffuse scattering (Born, 1942). This can be seen using laboratory or synchrotron X-ray sources as well as neutrons at large scale facilities (Osborn, 1990; Welberry, 2008). In principle such data can be used to reconstruct phonon dispersion curves at least for simple crystal structures and using model potentials (Holt, 1999). Diffuse scattering was among the early techniques used to obtain phonon dispersion curves along high symmetry directions in elemental crystals before inelastic neutron and X-ray

experiments became routine (Olmer, 1948; Placzek, 1954, Squires, 1978; Burkel 2000). Inelastic techniques using single crystals provide complete momentum and energy resolved dispersion curves, whilst diffraction only has momentum resolution. Interesting effects were noted by Willis *et al.* in the case of time-of-flight Laue neutron diffraction where the neutron can accidentally match the wavevector and energy of phonons leading to a splitting of the thermal diffuse scattering features corresponding to phonon emission and absorption (Willis *et al.* 1986; Schofield 1987). This effect has not been observed with X-rays due to the high energy of the order of several keV compared to up to hundreds of meV for lattice vibrations but in principle takes place as well. Willis derived a formalism to extract the sound velocity of a crystal using the splitting of the diffuse lines of the acoustic phonons which dominate the TDS pattern at least close to the Bragg peaks (Willis 1986). A few experiments were conducted to demonstrate the feasibility and good agreement was obtained for the sound velocity obtained by other means (Willis, 1986; Carlile and Willis, 1989; Carlile 1992). Inelastic effects have also been noticed in Quartz but were not considered further (Tucker, 2001). It should be noted though that only very few observations of direct phonon excitation in neutron diffraction experiments have been reported to date, limiting somewhat the use of this technique in particular for molecular crystals (Welberry, 2003).

Nowadays, density functional theory has established itself as a tool of choice to predict phonon dispersion curves from a crystal structure and is routinely used in the planning and interpretation of inelastic experiments (Mitchell *et al.*, 2005). These computations also give the phonon eigenvectors for arbitrary q-points which are not easily accessible experimentally though in principle available from the intensity of the TDS or inelastic peaks provided the inelastic structure factor differs from zero. Examples are now emerging where DFT computations are used to aid in the interpretation of diffuse scattering experiments (Bosak *et al.*, 2009; Wehinger *et al.*, 2014; Gutmann *et al.* 2013).

In this paper, we combine DFT calculations with the geometry of the Laue neutron diffraction experiment to compute the 'inelastic diffraction' associated with phonons. This is compared with diffuse scattering calculated in the instrument geometry using the quasi-static approximation, that is when the phonon energy is negligible compared to the energy of the scattering probe, and this is also compared with X-ray diffuse scattering. Our motivation is to be able to identify and reproduce the diffuse scattering arising from one-phonon scattering over a large region in reciprocal space in combination with ab-initio calculations in order to aid in the interpretation of diffuse scattering patterns beyond the Monte-Carlo modelling approach (Welberry, 2004)

1. Experimental

1.1. Diffraction experiments

NaCl single crystals with a purity of 99.99% were purchased from Sigma-Aldrich hereafter referred to as synthetic. A large irregularly shaped crystal was shaped into a sphere of 6mm diameter. This sample is usually used as a calibration standard to ensure reproducibility between ISIS experiment cycles. Natural specimens were obtained in Hallstatt (Austria) from the local salt mine. They had various colors, indicating impurities but also optically clear crystals. An optically clear, colorless crystal of approximate dimensions 2mm *4mm *5 mm was extracted. However, the purity is not known explicitly and hence data from the synthetic crystal are used throughout the paper. The natural sample was only used to verify that similar effects as described below occur and hence are sample independent although may vary in magnitude due to impurity effects on the phonons (Caldwell 1967). Neutron diffraction data were collected at room temperature using the SXD single crystal diffractometer at the ISIS spallation neutron source (Oxfordshire, UK, Keen *et al.*, 2006) on various occasions on the synthetic crystal with exposures ranging between 4 hours and up to 2 days at single settings or a series of crystal settings about 20 degrees apart. This crystal was also run at 20 K. The natural specimen was exposed for 12 hours in various orientations but only at room-temperature. Reciprocal space volumes from these data were obtained using SXD2001 (Gutmann, 2005). A natural crystal was also used for a complementary high-energy X-ray diffraction experiment on the beamline BW5 installed at the storage ring DORIS III at DESY in Hamburg, Germany. These data merely confirmed the absence of inelastic excitation effects seen in the neutron data.

1.1. Computation of phonon dispersions using DFT

Electronic-structure calculations were performed using the plane wave-pseudo-potential methods as implemented in the CASTEP code (Clark, 2005). The Perdew-Burke-Ernzerhof (PBE) (Perdew, 1996) generalised-gradient approximation (GGA) functional was used both for the plane-wave calculation and the generation of pseudopotentials. These were of the optimised norm-conserving variety (Rappe, 1990). Energies and forces were well-converged at a plane-wave cutoff of 600 eV. A Brillouin-zone (BZ) sampling of 8x8x8 q-points (60 points when symmetry-reduced) was found to be sufficient to converge energy and atomic forces below 2.2×10^{-8} eV/ion and 1.0×10^{-3} eV/Å, respectively. Sufficient self-consistent cycles were performed to achieve a convergence tolerance of 1.0×10^{-10} eV per atom. Geometry optimizations used the Broyden-Fletcher-Goldfarb-Shanno (BFGS) algorithm with a force tolerance of 1.0×10^{-3} eV/ Å. Phonon dispersion calculations were performed of the resulting minimum-energy structures via diagonalization of dynamical matrices computed using density-functional perturbation theory (DFPT) and linear-response methods (Refson, 2006) on a total of 60-q points. Because our intention was to enable the program to use output from either CASTEP or

VASP/PHONOPY, similar computations were also carried out with VASP (Kresse, 1994), which equally well reproduced the diffraction features. Throughout the paper, the CASTEP calculations are used.

2. Computation of the thermal diffuse scattering

We first establish a coordinate system in the neutron diffractometer based on spherical coordinates. The location of each pixel on the detector is characterised by two angles, δ and v which correspond to the longitude and latitude, respectively, as illustrated in Figure 1.
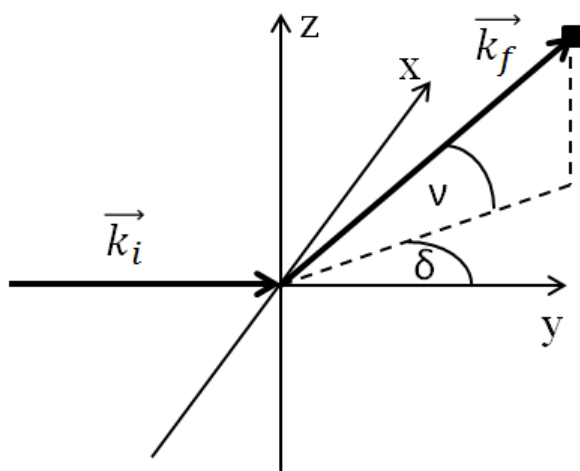

Figure 1: Coordinate system used to describe the scattering and instrument geometry.

The incident neutron beam is travelling along $\vec{k}_i$ which is along the positive y-direction and is scattered into a pixel located at the end-point of $\vec{k}_f$. Expressed in the left-handed orthonormal coordinate system (x,y,z) shown in Figure 1, the incident and scattered wavevectors read:

$$\vec{k}_i = \frac{2\pi}{\lambda_i}\begin{pmatrix} 0 \\ 1 \\ 0 \end{pmatrix} \qquad \vec{k}_f = \frac{2\pi}{\lambda_f}\begin{pmatrix} \sin(\delta)\cdot\cos(v) \\ \cos(\delta)\cdot\cos(v) \\ \sin(v) \end{pmatrix} \tag{1}$$

with λ_i and λ_f the wavelength of the incident and scattered neutron in Ångstrom, respectively. In the case of an elastic scattering event these have the same magnitude but generally differ in the case of inelastic scattering. Table 1 lists these angles for the 11 detector modules of the SXD

instrument and they are also graphically illustrated in Figure 2 for a NaCl data set at room-temperature.

The angular ranges for the δ and ν angles in Eq. 1 for the various detectors of the SXD instrument are listed in Table 1.

Table 1 List of angular ranges in unit of degrees for the various detector modules of the SXD instrument.

Detector module	δ (center +/-range)	ν (center +/- range)
1	142.5 +/- 23	0 +/- 23
2	90 +/- 23	0 +/- 23
3	37.5 +/-23	0 +/- 23
4	-37.5 +/- 23	0 +/- 23
5	-90 +/- 23	0 +/- 23
6	-142.5 +/- 23	0 +/- 23
7	90 +/- 37	-45 +/- 20
8	0 +/-37	-45 +/-20
9	-90 +/- 37	-45 +/- 20
10	-180 +/- 23	-45 +/- 20
11	0 +/- 180	-90 +/- 25

For a single crystal, the scattering vector $\vec{Q}$ is given as follows:

$$\vec{Q}=\vec{k}_f-\vec{k}_i = 2\cdot\pi\cdot[\omega]\cdot[\chi]\cdot[\varphi]\cdot[UB]\cdot\begin{pmatrix} h \\ k \\ l \end{pmatrix} \tag{2}$$

where $[\omega]$, $[\chi]$, and $[\varphi]$ denote rotation matrices corresponding to the angle settings of the goniometer stage, $[UB]$ the orientation matrix of the crystal and h,k,l are Miller indices, which need not be integer valued (Busing and Levy, 1967). For phonons it is convenient to decompose the h, k, l into an integer part, where Bragg reflection may occur, and a fractional part such that the latter reflects the wavevector of the phonon in the first Brillouin zone.
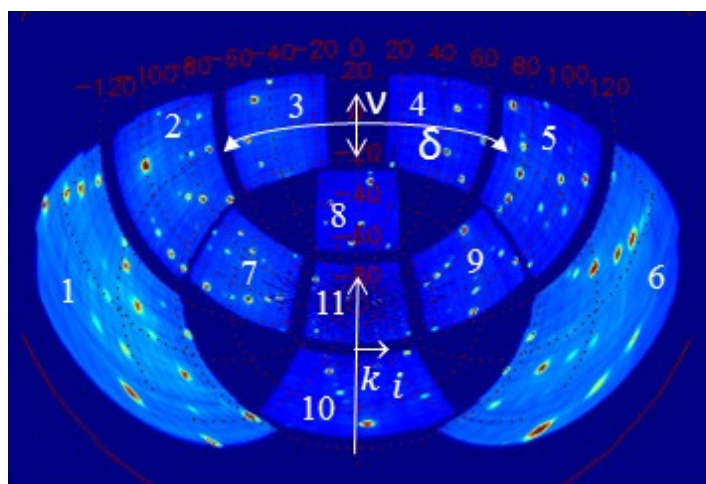
Figure 2: Illustration of the SXD detector geometry with detector module number labelling corresponding to Table 1 using a NaCl room-temperature data set integrated between a time-of-flight of 1500 and 10000 microseconds. The coordinate system corresponding to Figure 1 is superimposed as dotted grid lines.

In TOF neutron scattering, every pixel has a time-of-flight range associated with it, as a fixed histogram with a given number of time channels and a fixed minimum and maximum time. More recently event-mode has become available, where neutron events are time-stamped as they occur without imposing a histogram. The SXD instrument at ISIS uses the fixed histogram-mode. The time-of-flight recorded corresponds to the total travel time of the neutron from the source to the detector pixel and is measured in units of microseconds. The total travel time t_{tot} can be decomposed into the time from the source to the sample, t_i and the time from the sample to the pixel, t_f. These can be related to the wavelengths of the incident and scattered neutron:

$$\lambda_i = \frac{h \cdot t_i}{m_n \cdot L_1} \qquad\qquad \lambda_f = \frac{h \cdot t_f}{m_n \cdot L_2} \qquad\qquad (3)$$

where h is Planck's constant, m_n the neutron mass, L_1 and L_2 are the primary flight path from source to sample and secondary flight path from sample to the pixel, respectively, in mm. The energy of the neutron in meV is related to the wavelength as follows:

$$E = \frac{h^2}{2 \cdot m_n \cdot \lambda^2}$$

$$(4)$$

For calculating the TDS in the instrument geometry, every pixel and TOF channel is converted to E_f for a given E_i and the scattering vector $\vec{Q}$ which is transformed back to h,k,l using Eq. 1 and decomposed into an integer and fractional h,k,l in the first Brillouin zone in order to look up the eigenvectors and phonon frequencies at that point in the DFT output. We note that the DFT calculations sometimes use a reduced cell compared to the conventional crystallographic cell and hence a transformation between these two cells should also be applied when converting to h,k,l of the DFT cell.

For calculating first order TDS it is convenient to define a one-phonon structure factor (Xu, 2005):

$$F_j(\vec{Q}) = \sum_{k=1}^{n_{atoms}} \frac{b_k}{\sqrt{m_k}} e^{-u_k^2 \cdot Q^2/2} \cdot \left(\vec{Q} \cdot \vec{e}_{kj}(\vec{Q}) \right) \cdot e^{-i\vec{Q} \cdot \vec{R}_k} \qquad\qquad (5)$$

The summation extends over all n atoms, n_{atoms}, in the unit cell. Further, m_k is the mass of atom k, b_k its coherent scattering length, u_k^2 the mean square atomic displacement, taken as isotropic for the case of NaCl, $\vec{e}_{kj}(\vec{Q})$ the complex-valued eigenvector of atom k in the phonon mode j at wavevector $\vec{Q}$, and $\vec{R}_k$ the position of atom k in the unit cell. Here, unit cell refers to the primitive unit cell used by the DFT program. It should be noted that the form of Eq. 1 depends on whether the dynamical matrix in the DFT program is defined such as to give periodic eigenvectors, as is the case in CASTEP (Refson, 2006), or otherwise as is the case in PHONOPY (Togo, 2008). The formula given here applies to CASTEP. For the case of non-periodic eigenvectors see (Xu, 2005).

The TDS intensity can be written as follows assuming energy and momentum conservation are fulfilled:

$$I_{j+}(\vec{Q}) = C \cdot \frac{k_f}{k_i} \cdot \frac{1}{\omega_j} \left| F_j(\vec{Q}) \right|^2 \left(n(\omega_j, T) + 1 \right) \tag{6a}$$

$$I_{j-}(\vec{Q}) = C \cdot \frac{k_f}{k_i} \cdot \frac{1}{\omega_j} \left| F_j(\vec{Q}) \right|^2 n(\omega_j, T) \tag{6b}$$

with C=N/2, N being the number of atoms in the sample. This constant is treated as a scale factor and is set to 1 for convenience. ω_j denotes the frequency of the phonon mode j, and '+' and '-' refer to phonon creation and annihilation, respectively. The energy integration of the double-differential cross-section (6a, b) is effectively carried out here numerically using many wavelengths and counting the number of phonons falling into a given Q bin and normalising to this. The phonon occupancy at temperature T is given by:

$$n(\omega_j, T) = \frac{1}{e^{\hbar \omega_j / k_B T} - 1} \tag{7}$$

In the quasi-static approximation, (6a) and (6b) are summed over all n_{Modes} phonon modes to yield:

$$I(\vec{Q}) = const \cdot \sum_{j=1}^{n_{Modes}} \frac{1}{\omega_j} \cdot \left| F_j(\vec{Q}) \right|^2 \cdot \coth\left(\frac{\hbar \omega_j}{2 k_B T} \right) \tag{8}$$

The constant is treated again as a scale factor and set to 1. Initially a master mapping from pixel coordinates and TOF to a reciprocal space map is established, assuming only elastic events. This master mapping is essentially assigning a given pixel and TOF channel to a voxel in the reciprocal space volume. The recipe to compute inelastic diffraction can be summarised as follows:

1. Select a fixed wavelength/energy, λ_i and E_i and $\vec{k}_i$.

2. Compute for all pixels and TOF of the instrument λ_f, E_f and $\vec{k}_f$.

3. Compute $\vec{Q}=\vec{k}_f-\vec{k}_i$ as well as $\omega=E_f-E_i$ and use the experimental UB matrix for a given experimental run to derive h,k,l.

4. Transform h,k,l from the conventional crystallographic cell to the DFT cell, if necessary and decompose it into an integer part and fractional part in the first Brillouin zone.

5. Using the DFT phonons interpolated on a fine grid over the first Brillouin zone, check whether for the given h,k,l there is a matching phonon frequency corresponding to ω within a given tolerance in meV and compute the TDS intensity using eqs. (6a) or (6b) as appropriate and eq. (7). Add this to the reciprocal space voxel using the master map.

6. Repeat until all wavelengths are covered.

This receipe has been coded in OpenCL to enable parallel computation using multicore CPU's and GPU's.

3. Results

Sections through the (0,k,l) plane are shown in Figure 2 employing data from the high-angle, 90-degree and low angle banks. With reference to Figure 3 in (Keen *et al.*, 2006) which illustrates the detector numbering used in this paper, high-angle banks mean detectors 1,6, and 10, 90-degree banks detectors 2, 5, 7, 9 and 11, and low-angle banks 3, 4, and 8, respectively.

Diffuse scattering is concentrated close to the Bragg spots and takes the appearance of a butterfly shape. However, comparing the data from the various detectors, it becomes apparent that the diffuse scattering in the high-angle detectors near the Bragg spots is geometrically distorted rather than symmetric as would be expected. Weak arcs join or can be thought of as joining various neighbouring reflections on either side of the Bragg peak and these arcs are absent in the data from the low-angle banks. It should be noted that the indexation is taken as determined by the software. The assignement of which Miller index is h, k, or l merely corresponds to a permutation of the symbols and is not relevant for comparing the various data sets. Sections were chosen to provide as large a coverage as

possible. More complete volumetric data sets are available in the form of movies in the supplementary information.

NaCl phonons have been determined experimentally (Raunio, 1969) albeit over a somewhat limited reciprocal space and can quite easily be computed using state-of-the-art density functional codes such as CASTEP and VASP. NaCl is often included as an example tutorial for learning these programs with the resulting phonon dispersion curves closely matching the experimental ones. Due to the limited comparison and the fact that DFT phonons are calculated at 0K with no adjustable parameters, only qualitative agreement would be expected in our calculations below. In the absence of direct phonon excitations in the quasi-static treatment, the thermal diffuse scattering can be calculated as the sum over all the phonon branches at a given q-point using the formulas (5) and (8). It should be noted that in all calculations, only the diffuse scatterings is computed. Bragg peaks are not included as is commonly done when modelling diffuse scattering (Welberry, 2004).
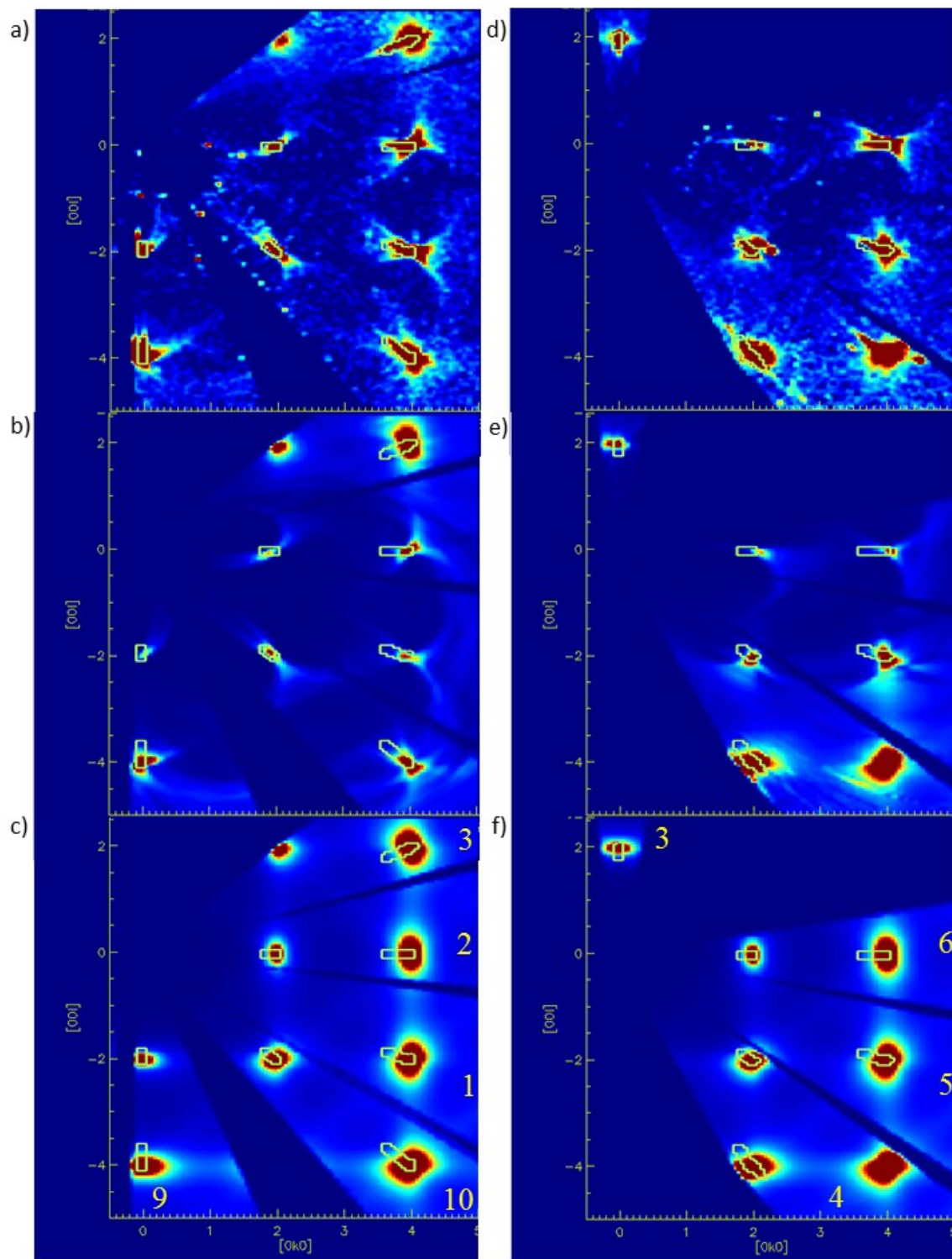

The presence of phonon dispersion curves in the data requires a different treatment. When creating the reciprocal space maps, the underlying assumption is that the scattering events are purely elastic, i.e. no energy transfer occurs and the initial and final momentum of the scattered neutron have the same magnitude. Either of these conditions are not fulfilled, when inelastic scattering takes place and this process is governed by energy and momentum conservation.

The computations were carried out in the detector geometry of the instrument and then mapped to crystallographic reciprocal space as a volumetric data set as outlined in section 3. Of the order of 5600 incident wavelengths were used from 560 meV down to 1 meV covering the time-of-flight range measured in a detector. The calculations were performed on Intel Xeon E5-2687 CPU's comprising effectively 32 cores. Despite parallelisation of the codes, the calculations were rather formidable. Computing a volumetric data set of 300 * 300 * 300 points took 24 hours per detector module and 5600 wavelengths. Three modules were computed in parallel and hence it would take of the order of 4 days to compute these volumetric data sets for all 11 detector modules and one orientation/temperature of the crystal. For comparison the TDS patterns took ~100 seconds per detector module. At this point, the codes have not been fully optimised for speed or memory and further gains are possible. For each wavelength, the phonon spectrum was calculated for both cases up- and down-scattering and all resulting maps were summed. Only inelastic events arising from exciting phonons from the ground-state and vice versa were considered. Events such as energy transfer between occupied phonon states, multiphonon scattering and higher harmonics, i.e. any processes involving more than one phonon were not included and did not appear essential as their contribution is thought to diminish rapidly. The resulting reciprocal space maps were not convoluted with the instrument resolution. The time-of-flight peak shapes are typically asymmetric along the

time-of-flight direction leading to a tail at the base of the peak that points towards the origin of reciprocal space giving the peaks a tear-drop shape in the reciprocal space maps. The footprint of the Bragg peaks is indicated by contours. These were derived from the 3D profile fitting routine in SXD2001 after transforming them to reciprocal space and taking a 1% contour level from the maximum of each peak. The contours were elongated in the radial direction to better capture the asymmetric tail. Trial runs were initially carried out to obtain a good value for the energy tolerance of 1 meV. It can be seen that both the standard TDS formalism and using our method of explicitly taking into account direct phonon excitations resembles the data recorded with the low-angle bank, corresponding to detector 3 in Figure 3 a)-c). However, for the 90-degree (detectors 2,9 in Figure 3 a)-c)) and backscattering data (detectors 1 and 10) using the latter formalism results in a qualitatively better agreement compared to the TDS formalism with the observed diffuse scattering. A more complete illustration of the inelastic effects as they occur throughout reciprocal space and away from the (0, k, l) layer is contained in the movies in the supplementary information. It was already noted by (Willis, 1986) that inelastic effects would best be seen in backscattering.

To further ascertain the phonon origin of the scattering leading to the splitting of diffuse lines two more experiments were conducted. In one, the same synthetic specimen was measured at room-temperature in a different orientation by rotating the crystal around a vertical axis from $\omega=-150°$ to $+150°$ and the diffuse scattering calculated accordingly using the full phonon dispersions and the quasi-static approach. The results are shown in Figure 3 d)-f). Again, the diffuse scattering computed using the inelastic treatment shows better agreement. This illustrates that the diffuse features change appearance in the presence of inelastic effects as the crystal is rotated, whilst no changes are expected when using the quasi-static approximation. The former is expected, since upon rotating the crystal, a given feature in reciprocal space is probed with neutrons of a different wavelength and hence energy. Intuitively, this can be understood from Bragg's law: Given a constant d-spacing, when changing the scattering angle θ, the wavelength has to change. A similar effect is also seen in (Welberry, 2003), comparing Figures 3.a) and 5.a). The angular dependence of this effect is discussed rather more formal in the paper of (Schofield 1987). Indeed, if the diffuse scattering changes appearance and diffuse lines appear split when measured in different orientations, this observation can be taken as an indication as arising from excitations in the sample rather than static lattice distortions. The second experiment used again the synthetic crystal in a somewhat different orientation compared to the room-temperature measurement but this time the crystal was cooled to 20K and the calculations carried out using this temperature and an energy tolerance of 1 meV. It is expected that this would change the population of the phonons leading to a more pronounced asymmetry in the intensity distribution of the features corresponding to the phonon excitation and annihilation. The results are shown in Figure 4. The differences between the calculated patterns using the TDS and our approach in the (0kl)-layer

(Figures 4. a)-c) are a bit more subtle and from a comparison with the experimental data it appears not clear which would be preferred. In comparison, the (4kl)-layer contains stronger diffuse features and again the inelastic treatment is clearly favoured. The intensity scales are the same as in Figure 3. This allows assignment of the arc like features on the higher and lower Q side of a Bragg peak to phonon emission and absorption, respectively. The supplementary movie S2 shows a side-by-side comparison of the 20K data and calculations for a volumetric data set. Finally, we note that the inelastic effects break the symmetry of the diffraction pattern and hence averaging of the diffuse scattering using the Laue symmetry of the crystal structure as is commonly done in single-crystal diffuse scattering experiments should be avoided in this case.

Figure 3: Comparison of the (0kl) layer between experiment and theory. a)Experimental data from the synthetic NaCl crystal at room-temperature recorded in one orientation. Contour lines are guides to the eyes for the shape of the Bragg peaks at the base of the peaks, b) computation of phonon excitations, c) thermal diffuse scattering in the quasi-static approximation. d), e), f) are like a), b), c) for the same NaCl specimen. The numbers in c) and f) refer to the detector bank contributing to this section and correspond to the labelling in figure 2.
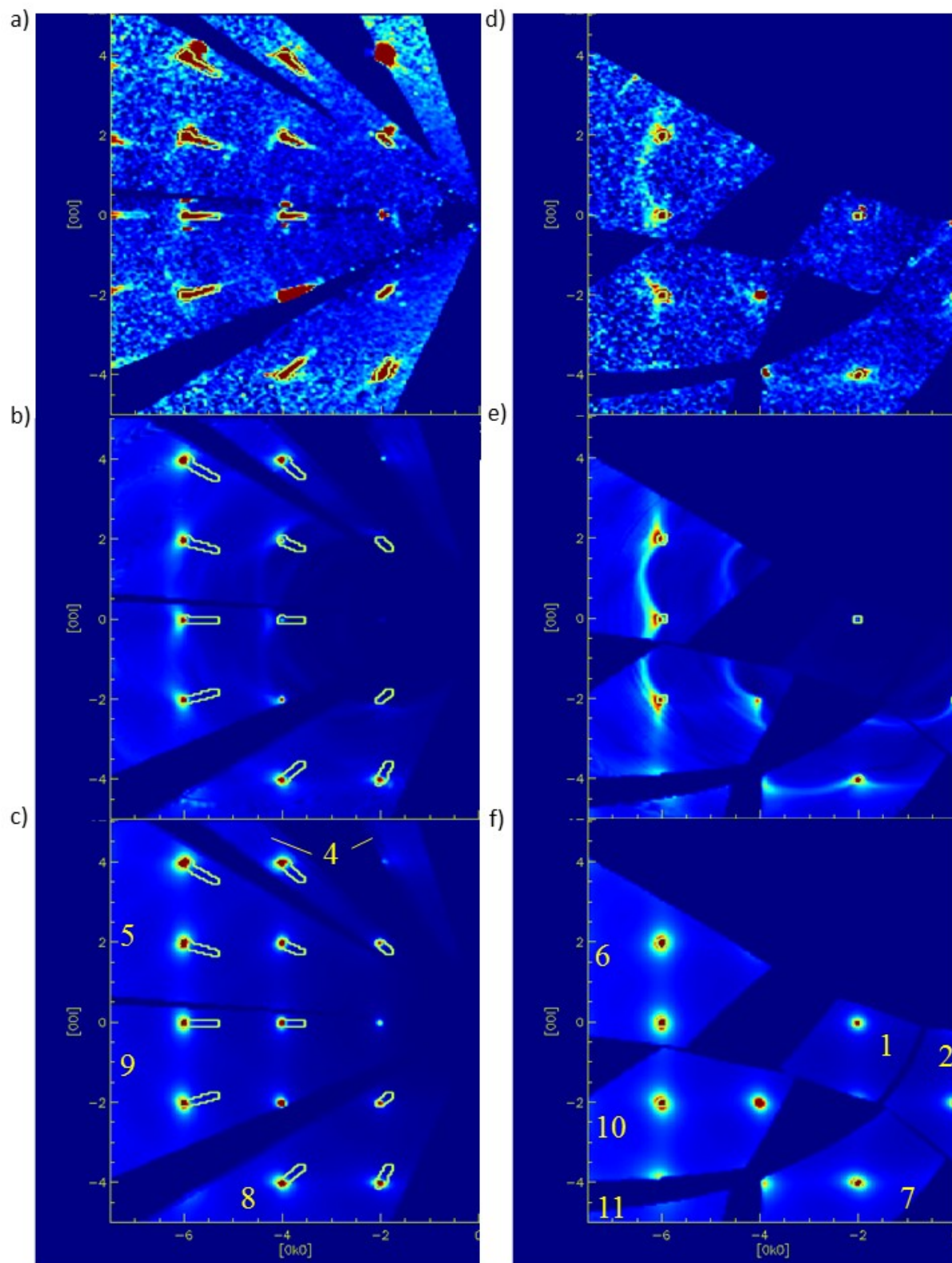
Figure 4: Comparison of the (0kl) layer between experiment and theory: a) Experimental neutron data of the synthetic NaCl crystal at 20K, b) theoretical calculation using inelastic events at a temperature of 20K, c) thermal diffuse scattering in the quasi-static approximation. d), e), f) are like a), b), c), respectively but for the (4kl)-layer.

4. **Summary and conclusions**

In this paper, we have illustrated the effect of inelastic excitations that can occur in a time-of-flight neutron single crystal Laue experiment. The signal arising from TDS takes the form of split arcs originating from Bragg reflections and this is most pronounced in the data from the back-scattering banks whilst virtually absent in the low-angle detectors. The consequence is the breaking of the symmetry of the diffraction pattern which means that such data should not be symmetrised using the Laue symmetry as is commonly done. Furthermore, recording of the diffuse scattering at a much lower temperature results in a pronounced asymmetry in the intensities of the diffuse split arcs on the high and low Q side of Bragg reflections due to the change in the phonon population. The effects have been computed combining the TDS formulas for the inelastic scattering with phonon eigenvectors and frequencies as well as the temperature and simulating the experiment in the actual instrument geometry using many wavelengths as a discretised representation of the incident white beam. Whilst such effects may be considered a nuisance when modelling diffuse scattering using a Monte-Carlo approach (Welberry, 2004), they can help in augmenting the information and classifying diffuse features with respect to their dynamic or static origin (Welberry, 2003). If ab-initio phonons or magnons in case of magnetic diffuse scattering are available these can be used to aid in the interpretation of such features and contrasting them from diffuse scattering arising from other types of disorder. In the case of magnons, polarised neutrons can further establish their magnetic origin (Brückel, 2002). In the absence of sufficiently large single crystals for inelastic neutron scattering, this can also be regarded as a means to test the ab-initio results against diffraction data, particularly since in our approach we can choose an energy tolerance for the phonon frequencies. Since more instruments similar to SXD are now operational at other spallation neutron sources such as TOPAZ at the Spallation Neutron Source (Oak Ridge National Laboratory, USA) or SENJU at J-PARC (Ibaraki Prefecture, Japan) it is anticipated that such inelastic features will increasingly be observed (Schultz, 2014; Tamura, 2012). It can also be used complementarily to neutron powder inelastic experiments or optical spectroscopies such as IR, UV-VIS and Raman. Finally, as further extensions of this work one may envisage using such effects to fit either model potentials as done by (Holt, 1999) or coupling this with DFT to derive better model potentials, possibly including other kinds of spectroscopic data as well. The computational effort in the current work for our method and the DFT calculations on top of this seem rather discouraging for the time being but this may change sometime in the future with growing computing power.

References

Born, M. and Lonsdale, K. (1941), *Nature* **150**, 490.

Bosak, A., Hoesch, M., Krisch, M. Chernyshov, D. Pattison, P., Schulze-Briese, C., Winkler, B., Milman, V., Refson, K., Antonangeli, D., and Farber, D. (2009), *Phys. Rev. Lett.* **103**, 076403.

Brückel, T. and Schweika, W. (2002), *Polarized Neutron Scattering*, Forschungzentrum Jülich GmbH, ISBN 3-89336-314-9.

Burkel, E. (2000), *Rep. Prog. Phys.* **63**, 171 - 232.

Busing, W. R. and Levy, H. A. (1967), *Acta Cryst.* **22**, 457 - 464.

Caldwell, R. F and Klein, M. V. (1967), *Phys. Rev.* **158**, 851 – 874.

Carlile, C. J., Keen, D. A, Wilson, C. C., and Willis, B. T. M. (1992), *Acta Cryst.* A**48**, 826 - 829.

Carlile, C. J. and Willis, B. T. M. (1989), *Acta Cryst.* A**45**, 708 - 715.

Clark, S. J., Segall, M. D., Pickard, C. J., Hasnip, P. J., Probert, M. J., Refson, K., and Payne, M. C. (2005), *Z. Kristallogr.* **220**, 567 – 570.

Ellis, P. J. and Bernstein, H. J. (2012), http://www.bernstein-plus-sons.com/software/CBF/.

Gutmann, M. J. (2005), *SXD*2001. ISIS Facility, Rutherford Appleton Laboratory, Oxfordshire, England.

Gutmann, M. J., Refson, K., von Zimmermann, M., Swainson, I. P., Dabkowski, A. and Dabkowska, H. (2013), *J. Phys. Cond. Mat.* **25**, 315402.

Holt, M., Wu, Z., Hong, H., Zschack, P, Jemian, P. Tischler, J. Chen, H. and Chiang, T.-C. (1999), *Phys. Rev. Lett.* **83**, 3317 - 3319.

Kabsch, W. (2010), *Acta Cryst.* D**66**, 125 – 132.

Keen, D. A., Gutmann, M. J., and Wilson, C. C. (2006), *J. Appl. Cryst.* **39**, 714 - 722.

Mitchell, P. C. H., Parker, S. F., Ramirez-Cuesta, A. J., Tomkinson, J. (2005) *Vibrational spectroscopy with neutrons*, World Scientific.

Kresse, G. and Hafner, J. (1994), *Phys. Rev. B* **49**, 14251 – 14269.

Olmer, P. (1948), *Acta Cryst.* **1**, 57 - 63.

Osborn, J. C. and Welberry, T. R. (1990), *J. Appl. Cryst.* **23**, 476 - 484.

Placzek, G. and Van Hove, L. (1954), *Phys. Rev.* **93**, 1207 - 1214.

Perdew, J. P., Burke, K., and Ernzerhof, M. (1996), *Phys. Rev. Lett.* **77**, 3865 – 3868.

Rappe, A. M., Rabe, K. M., Kaxiras, E., Joannopoulos, D. (1990), *Phys. Rev. B* **41**, 1227 – 1230.

Raunio, G., Almqvist, L. and Stedman, R. (1969), *Phys. Rev.* **178**, 1496 – 1501.

Refson, K., Tulip, P. R., and Clark, S. J. (2006), *Phys. Rev. B* **73**, 155114.

Schofield, P. and Willis, B. T. M. (1987), *Acta Cryst.* A**43**, 803 - 809.

Schultz, A. J., Jørgensen, M. R. V., Wang, X., Mikkelson, R. L., Mikkelson, D. J., Lynch, V. E., Peterson, P. F., Green, M. L, and Hoffmann, C. M. (2014), *J. Appl. Cryst.***47**, 915 – 921.

Squires, G. (1978), *Introduction to the theory of thermal neutron scattering*, Cambridge University Press.

Tamura, I., Oikawa, K., Kawasaki, T., Ohhara, T., Kaneko, K., Kiyanagi, R., Kimura, H., Takahashi, M., Kiyotani, T., Arai, M. Noda, Y., and Ohshima K. (2012), *J. Phys.: Conf. Ser.* **340**, 012040.

Togo, A., Oba, F. and Tanaka, I. (2008), *Phys. Rev. B* **78**, 134106.

Tucker, M. G., Keen, D. A., and Dove, M. T. (2001), *Miner. Mag.* **65**, 489 – 507.

Wehinger, B., Bosak, A., Piccolboni, G., Refson, K., Chernyshov, D., Ivanov, A., Rumiantsev, A., and Krisch, M. (2014), *J. Phys. Cond. Mat.* **26**, 115401.

Welberry, T. R., Goossens, D. J., David, W. I. F., Gutmann, M. J., Bull, M. J, and Heerdegen, A. P. (2003), *J. Appl. Cryst.* **36**, 1440 - 1447.

Welberry, T. R. (2004), *Diffuse X-ray Scattering and Models of Disorder*, Oxford University Press.

Welberry, T. R., Goossens, D. J., Heerdegen, A. P., and Lee, P. L. (2005), *Z. Kristallogr.* **220**, 1052 – 1058.

Welberry, T. R. and Goossens, D. J. (2008), *Acta Cryst.* A**64**, 23 - 32.

Willis, B. T. M., Carlile, C. J., Ward, R. C., David, W. I. F., and Johnson, M. W. (1986), *Europhys. Lett.* **2**, 767 - 774.

Willis, B. T. M. (1986), *Acta Cryst.* A**42**, 514 - 525.

Xu, R. and Chiang, T.-C. (2005), *Z. Kristallogr.* **220**, 1009-1016.

Figure 1   Coordinate system used to describe the scattering and instrument geometry.

Figure 2   Illustration of the SXD detector geometry with detector module number labelling corresponding to Table 1 using a NaCl room-temperature data set integrated between a time-of-flight of 1500 and 10000 microseconds. The coordinate system corresponding to Figure 1 is superimposed as dotted grid lines.

Figure 3   Comparison of the (0kl) layer between experiment and theory. a)Experimental data from the synthetic NaCl crystal at room-temperature recorded in one orientation. Contour lines are guides to the eyes for the shape of the Bragg peaks at the base of the peaks, b) computation of phonon excitations, c) thermal diffuse scattering in the quasi-static approximation. d), e), f) are like a), b), c) for the same NaCl specimen. The numbers in c) and f) refer to the detector bank contributing to this section and correspond to the labelling in figure 2.

Figure 4   Comparison of the (0kl) layer between experiment and theory: a) Experimental neutron data of the synthetic NaCl crystal at 20K, b) theoretical calculation using inelastic events at a temperature of 20K, c) thermal diffuse scattering in the quasi-static approximation. d), e), f) are like a), b), c), respectively but for the (4kl)-layer.

Supporting information

Figure S1   Comparison of experimental (left) and computed inelastic diffraction (right) at room-temperature. A layer-by-layer scan through a reciprocal space volume is shown.

Figure S2   Comparison of experimental (left) and computed inelastic diffraction (right) at room-temperature. A layer-by-layer scan through a reciprocal space volume is shown.